POLITECNICO DI TORINO
Repository ISTITUZIONALE

Advanced Control of GaN Y-Inverter for Traction Motors

Original
Advanced Control of GaN Y-Inverter for Traction Motors / Campanelli, F., Mandrile, F., Rubino, S., Armando, E., Bojoi, R.. - In: IEEE OPEN JOURNAL OF INDUSTRY APPLICATIONS. - ISSN 2644-1241. - (2026), pp. 1-14. [10.1109/ojia.2026.3707657]

Availability:
This version is available at: 11583/3012633 since: 2026-10-18T13:05:48Z

Publisher:
IEEE

Published
DOI:10.1109/ojia.2026.3707657

Terms of use:

This article is made available under terms and conditions as specified in the corresponding bibliographic description in the repository

Publisher copyright

(Article begins on next page)

19 November 2026

IEEE Open Journal of
Industry Applications

Received 30 January 2026; revised 13 April 2026; accepted 23 June 2026. Date of publication 25 June 2026;
date of current version 8 July 2026.

Digital Object Identifier 10.1109/OJIA.2026.3707657

Advanced Control of GaN Y-Inverter for Traction Motors

FEDERICO CAMPANELLI (Student Member, IEEE), FABIO MANDRILE (Member, IEEE), SANDRO RUBINO (Senior Member, IEEE), ERIC ARMANDO (Senior Member, IEEE), AND RADU BOJOI (Fellow, IEEE)

Department of Energy "Galileo Ferraris", Politecnico di Torino, 10129 Turin, Italy

CORRESPONDING AUTHOR: FEDERICO CAMPANELLI (e-mail: federico.campanelli@polito.it).

ABSTRACT The cascaded buck–boost Y-inverter is a promising DC–AC converter topology due to its capability to accept a wide input DC voltage range while producing near-sinusoidal output AC voltages. The advantages of the Y-inverter can also be leveraged for electrified powertrains fed by fuel cells. As the power levels of such powertrains may exceed hundreds of kW, it is essential to minimize the size of the reactive elements required by the Y-inverter. This aim can only be achieved by increasing the switching frequency. By leveraging the unprecedented switching performance of gallium-nitride (GaN) transistors. The control solutions available in the literature for the Y-inverters are mostly based on a conventional cascaded voltage and current control, employing proportional–integral (PI) controllers in stationary frames. However, these solutions have limited bandwidth performance when the switching frequency is roughly lower than one hundred kHz, as may occur for traction inverters. Therefore, this article proposes an advanced control that is tailored for high-performance torque control of traction motors fed by GaN Y-inverters. It exploits rotating reference frames for voltage control and deadbeat control to enhance the dynamic control performance. The proposed solution has been successfully tested on a reduced-scale GaN Y-inverter supplying a permanent magnet synchronous motor for light traction.

INDEX TERMS Current control, deadbeat control, electric vehicles, gallium-nitride (GaN) converters, synchronous motor drives, torque control, traction, voltage control, Y-inverter.

I. INTRODUCTION

The new generations of electric vehicles (EVs) require new technologies to fulfill the market expectations. While batteries are the primary power source, there is growing interest in fuel cell (FC) electric vehicles due to hydrogen's high energy storage capability [1]. However, the output voltage of FCs is relatively low (below 200 V) and therefore not suitable for most EVs. Moreover, the FC output voltage exhibits a much wider voltage range with a value that is strongly dependent on the load current [2].

Therefore, a DC–DC converter is usually employed to boost the FC's output voltage to the levels required by the traction voltage source inverter (VSI) and the electric motor. This conventional solution (DC–DC converter and VSI) is expensive, as the installed power is doubled compared to the battery solution. Moreover, the efficiency is also reduced due to the losses into the cascaded power conversion units.

The Y-inverter using gallium-nitride (GaN) devices offers a promising alternative to the conventional solution of a two-level VSI fed by a DC–DC converter. Originally proposed for low-power FC compressors [4] and also for grid-connected converters [5], [6], [7], it has three identical units; each unit consists of a cascaded buck cell and a boost cell, as shown in Fig. 1.

The Y-inverter has the following several advantages.

1) It accepts a wide range of input voltages provided by FCs or from batteries with a limited number of cells.
2) It offers higher efficiency compared to the conventional solution (DC–DC converter and VSI) since the buck cells and the boost cells do not switch simultaneously [8], [9]. Moreover, discontinuous conduction mode modulation can be implemented for the switching cells [10], [11].

© 2026 The Authors. This work is licensed under a Creative Commons Attribution 4.0 License. For more information, see https://creativecommons.org/licenses/by/4.0/

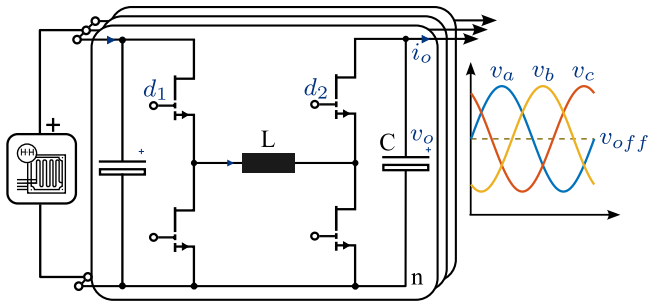


FIGURE 1. Y-VSI inverter concept [3] obtained as three identical units consisting of cascaded buck and boost switching cells.

3) It provides a capacitive output, allowing the converter to be positioned far from the electrical machine [12] and enabling simple parallelization of the converter to increase the output power [13].
4) It provides a near-sinusoidal voltage to the motor, reducing losses and eliminating the high dv/dt stress on motor windings seen with traditional VSIs, removing the need for three-phase filters in the output [14].

The design of the Y-inverter for high-power density applications [15] requires high switching frequencies to minimize the volume of reactive elements [16], [17], [18]. Therefore, wide-bandgap semiconductor technologies, such as silicon carbide or GaN [19], [20], [21], [22], [23], must be considered.

When compared with a conventional two-level VSI, the control of the Y-inverter is more complex and challenging due to the additional states introduced by the additional reactive elements, i.e., inductor L and output capacitors C. The most prominent Y-inverter control solution that has been proposed in the literature is a cascaded scheme with three outer voltage loops (to control the output capacitor voltages) and three inner current control loops (to control the inductor currents), using conventional proportional–integral (PI) controllers [3]. This solution has been proposed for a low-power GaN Y-inverter switching at 300 kHz and implemented on a field-programmable gate array (FPGA). The high-power traction motors (hundreds of kW) require fundamental frequencies exceeding the kHz [24], while the adopted switching frequencies are usually limited to about 100 kHz. Moreover, the control algorithm would ideally be implemented using microcontrollers, rather than FPGAs, for cost reasons.

The literature reports just a few attempts in considering the Y-inverter for traction applications [11], [12], [25], but without a complete experimental verification of a true torque control of a traction motor.

Previous literature works focused on hardware design [8], simple cascaded PI controllers in stationary coordinates [3], or grid-connected converters dealing with relatively slow frequencies [7]. Thus, closed-loop controls at elevated frequencies with respect to the switching frequency have not been explored as of yet. Therefore, this article proposes a novel voltage and current control solution for traction

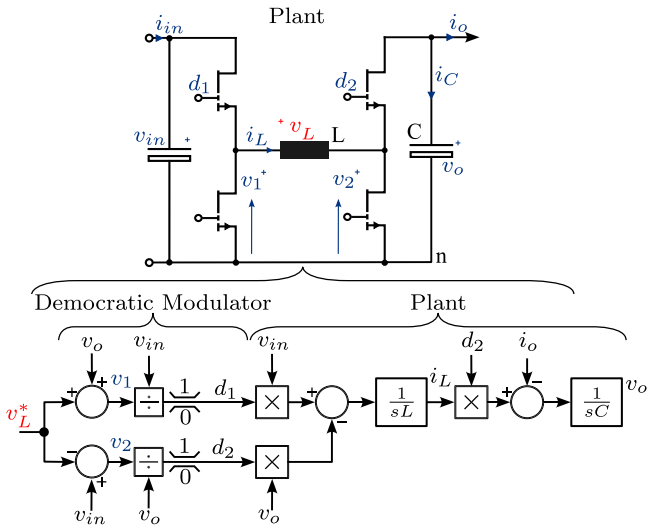


FIGURE 2. Single phase PEBB of the Y-inverter with dynamic model of the plant.

Y-inverters designed to meet the demanding torque control requirements of EV motors. The proposed method combines deadbeat predictive current control with PI voltage regulators in a rotating reference frame, achieving high voltage bandwidth at reasonable GaN switching frequencies, compatible with the power levels required by traction inverters. This article extends the conference paper [26] by providing an exhaustive experimental validation of an electrical drive consisting of a GaN Y-inverter prototype that supplies a torque-controlled interior permanent magnet (IPM) motor, specifically designed for light traction applications. According to the literature, this work is one of the first presenting true torque control using the Y-inverter.

The rest of this article is organized as follows. Section II describes the Y-inverter topology and the related state-space model, Section III details the proposed control diagram, and Section IV presents simulation and experimental results. Finally, Section V concludes this article.

II. Y-INVERTER TOPOLOGY ANALYSIS

The Y-inverter has been described in detail in the literature [3], [5], [6], [7], [8], [9], so only its main operating principles are briefly summarized in this section. The Y-inverter comprises three identical power-electronic building blocks (PEBBs). A single PEBB conversion unit is shown in Fig. 2 and consists of two cascaded bidirectional switching cells, hereafter named buck and boost cells, respectively, interconnected via an inductor L. A three-phase load is connected at the capacitive output terminals of the three PEBB units. In Fig. 2, d_1 is the duty cycle of the upper transistor of the buck switching cell, while d_2 is the duty cycle of the upper transistor of the boost switching cell. The individual switching functions of transistors are obtained through single carrier-based comparison (not shown here for simplicity). Each PEBB operates independently, enabling the synthesis of an output voltage waveform

characterized by a superposition of a DC bias and a sinusoidal AC component, as qualitatively represented in Fig. 1. To avoid the circulation of DC components in the load, the three DC components must be equal over a fundamental AC period. If the application requires it, it is possible to increase the power level of the Y-inverter by connecting in parallel more than one PEBB per phase. This is thanks to the inherent inductor L of the topology; the current control shall split the current evenly among the interleaved PEBBs. This is a scope of future research.

The pulsewidth modulation (PWM) strategy adopted in this work is the "democratic modulator" that is described in detail in [3]. This technique employs a comparative analysis between the input DC voltage v_{in} and the desired output voltage $v_{o,abc}$. Based on this comparison, the control algorithm selectively activates either the buck or boost cell of each PEBB unit. Specifically, the boost cell switches when the output voltage exceeds the input DC voltage, while the buck cell is operated with $d_1 = 1$. When the output voltage is lower than the input DC voltage v_{in}, the buck cell is switching, while the buck cell is operated with $d_2 = 1$ [3]. Therefore, only one cell is switching, allowing a drastic reduction of the switching losses [3]. Owing to the unequal duty intervals of the buck and boost legs over the fundamental period, the corresponding RMS currents and switching losses are generally not identical, which may lead to unequal thermal stress; a detailed treatment of this design aspect is given in [9]. Fig. 2 also provides the second-order dynamic model of each conversion PEBB unit, where the state variables are the inductor current i_L and the output voltage v_o with respect to the reference potential n.

The PEBB model is described as in (1), the approximations derived for this representation include the ideal average model of the bidirectional switching cell, ideal and linear passive components (L and C), and no PWM-induced aliasing and discretization. This form allows the ideal plant characterization in its dynamical form. Distortions, PWM delays, measurement inaccuracies, and parameter deviation will be discussed later on in the article

$$\begin{cases} L \cdot \dot{I}_L = d_1 \cdot V_{IN} - d_2 \cdot V_o \\ C \cdot \dot{V}_o = d_2 \cdot I_L - I_o. \end{cases} \tag{1}$$

The canonical form for linear systems can be represented as the continuous-time variant representation following the form of (2):

$$\left[\dot{x(t)}\right] = A(t) \cdot [x(t)] + B(t) \cdot [y(t)]. \tag{2}$$

where A is the system's matrix, B is the input matrix, $x(t)$ the state vector, and $y(t)$ the output vector. Following this notation, the model (1) can be expressed in the canonical form of linear systems, as shown in the following equation:

$$\begin{bmatrix} \dot{I}_L \\ \dot{V}_o \end{bmatrix} = A \cdot \begin{bmatrix} I_L \\ V_o \end{bmatrix} + B \cdot \begin{bmatrix} V_{IN} \\ I_o \end{bmatrix} \tag{3}$$

where the state-space matrices A and B are computed as in (4). The output of the system consists of the states vector in this work, following the state-space representation nomenclature [27]:

$$A = \begin{bmatrix} 0 & -\frac{d_2}{L} \\ \frac{d_2}{C} & 0 \end{bmatrix}, B = \begin{bmatrix} \frac{d_1}{L} & 0 \\ 0 & -\frac{1}{C} \end{bmatrix}. \tag{4}$$

This state-space model forms the foundation for the deadbeat predictive control described in the following section.

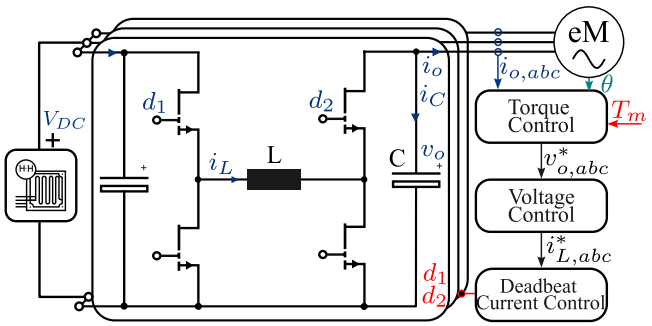


FIGURE 3. Overview of the proposed Y-inverter cascaded control.

III. Y-INVERTER CASCADED CONTROL

The proposed Y-inverter control scheme for traction drives has the three-layer structure shown in Fig. 3. The outermost layer is the torque control for the traction motor [28], which can implement any torque controller solution available in the literature. The torque control inputs are the reference torque T_m^*, the measured phase currents $i_{o,abc}$, and the rotor position θ_m. At the same time, the outputs of the torque controller are the three reference phase voltages ($v_{o,abc}$) of the Y-inverter. These reference voltages constitute the voltage control inputs, representing the second layer. The outputs of the voltage control are the reference currents ($i_{L,abc}$) of the Y-inverter inductors, which are the input of the third control layer, namely, deadbeat current control. This inner layer calculates the inductor voltages ($v_{L,\text{abc}}$), which are then used by the "democratic modulator" to determine the duty cycles (d_1 and d_2) for each converter unit, as described in [3].

The complete voltage and current control architecture is represented in Fig 4. The voltage control is implemented with PI controllers in a rotating frame, ensuring zero steady-state error. On the other hand, the deadbeat current controller ensures a fast dynamic response of the inductor current.

A. VOLTAGE CONTROL

The voltage control loop is implemented with PI regulators to manage the output capacitor voltages. Compared to the solutions reported in the literature [4], this work proposes the implementation of PI regulators operating in rotating coordinates synchronous with the motor speed. This way, the voltage components required by the torque controller v^*_{abc} are imposed without steady-state error, ensuring dynamic and steady-state torque regulation accuracy. For convenience, the rotor dq coordinates of the motor are chosen in this work.

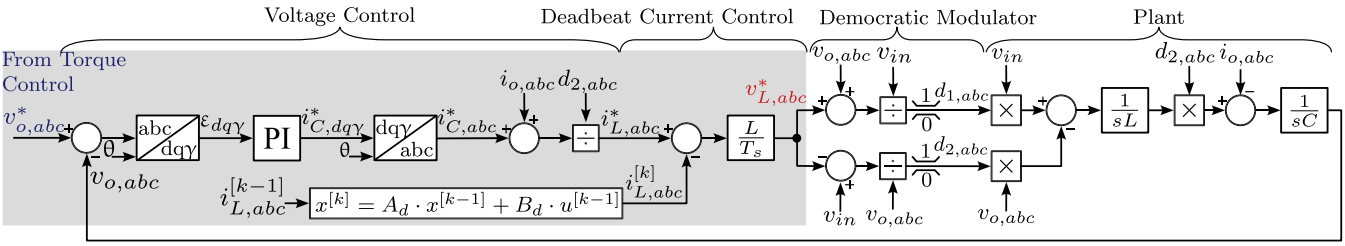


FIGURE 4. Block diagram of the proposed control architecture.

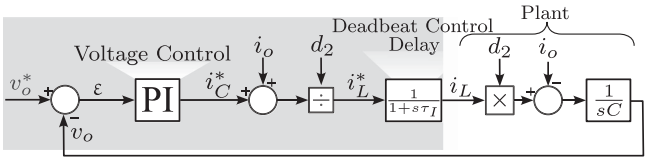


FIGURE 5. Block diagram of the voltage control loop.

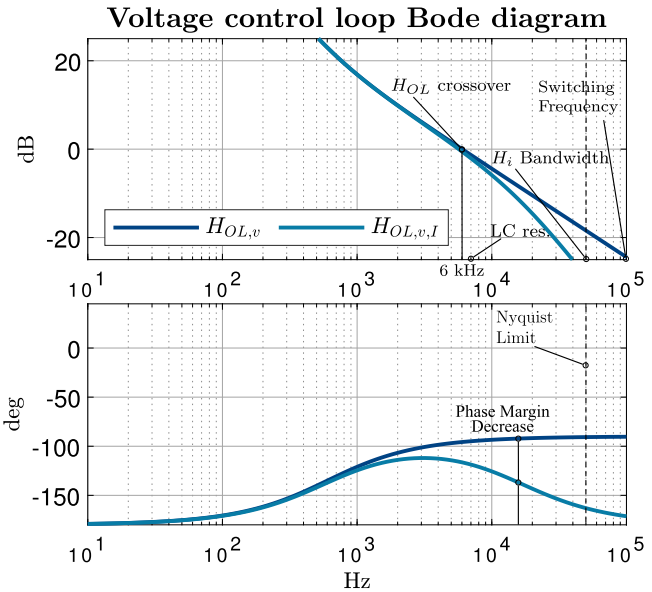


FIGURE 6. Voltage control loop Bode diagram: open-loop transfer function with $H_{OL,v,I}$ and without $H_{OL,v}$ deadbeat delay.

However, the homopolar voltage component, hereafter called v_γ, must also be controlled. Therefore, the input reference voltages $v_{o,abc}$ for the voltage control are computed, as shown in the following equation:

$$v^*_{o,abc} = v^*_{abc} + v^*_\gamma. \tag{5}$$

Regarding the reference of the homopolar voltage component v^*_γ, multiple choices are allowed. The criteria for imposing the homopolar component equal to the necessary DC bias are to avoid negative output capacitor voltages. The DC bias can consist of the amplitude of the reference voltages required by the torque controller v^*_{abc}. Alternatively, the DC bias can be set equal to half of the maximum output voltage by converter design.

On the other hand, the reference homopolar voltage can consist of the DC bias plus the common mode voltage injection typically adopted in conventional three-phase VSI to extend the linearity of the AC voltage output, e.g., space vector modulation or other PWM techniques reported in the literature.

The outputs of the PI regulators $i^*_{C,dq\gamma}$ are then expressed in phase coordinates *abc* using the inverse Park transformation, yielding the three reference capacitor currents $i^*_{C,abc}$. In order to compute the reference inductor's current $i^*_{L,abc}$, the following consecutive actions are performed. First, the reference output current of the boost switching cell is computed by adding, as feedforward, the measured motor currents $i_{o,abc}$ to the reference capacitor currents $i^*_{C,abc}$. Subsequently, the reference inductors' currents $i^*_{L,abc}$ are computed from the reference output current of the boost switching cell according to the reference duty cycle $d^*_{2,abc}$ (see Fig. 5).

To correctly represent the dynamical system of the voltage control loop, it is necessary to know that the proposed deadbeat current controller introduces a delay of two steps between reference and actuation [27]. This delay, τ_I, can be modeled in the system's transfer function as a time delay that is approximately equal to twice of the sampling period T_s, i.e., equal to the switching period T_{sw} in this work. Although the literature reports several Laplace domain representations for digital PWM delays [29], a simplified first-order low-pass filter model can be considered sufficient. This approximation is justified since there is a significant bandwidth difference between the deadbeat current control and the voltage PI-based control.

The Laplace block diagram of the equivalent voltage control loop is shown in Fig. 5 and includes the delay introduced by the deadbeat current control. To properly design the gains of the PI voltage regulators, it is necessary to take this delay into account. Proof of this is shown in Fig. 6, reporting the effect of the delay in terms of a Bode diagram. In detail, Fig. 6 shows the equivalent open-loop transfer function of the voltage control loop with ($H_{OL,v,I}$) and without considering ($H_{OL,v}$) the delay τ_I, respectively.

The figure reports the switching frequency of 100 kHz that was used by the Y-inverter. The current control equivalent bandwidth (H_i) is also shown as half of the switching frequency, as is typical for deadbeat controls. The *LC* self-resonance frequency f_{LC} of the Y-inverter is 6.8 kHz and it was also reported for clarity. The ratio of H_i/F_{LC} is above 7, which gives the current control enough margin to dampen

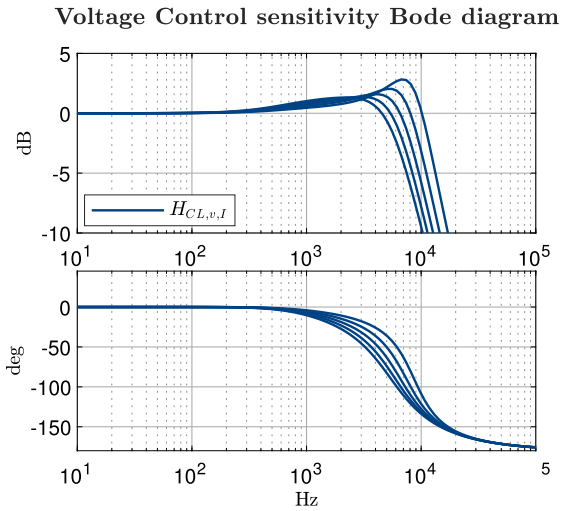


FIGURE 7. Capacitor parameter drift influence on voltage loop Bode diagram.

the resonances induced in the *LC* system. The final adopted bandwidth of the voltage control was chosen as 6 kHz.

It is noted that the delay introduces an additional attenuation of 20 dB/dec with a slope change from −20 to −40 dB/dec. Moreover, the delay introduces a reduction of the phase margin at the crossover frequency (see Fig. 6). Therefore, when accounting for the two-step delay, the complete open-loop transfer function takes the form, as shown in the following equation:

$$H_{OL}(s) = \frac{v_o}{\varepsilon} = \frac{s \cdot k_p + k_i}{s^2 \cdot C} \cdot \frac{1}{1 + s\tau_I}. \tag{6}$$

The zero of the PI regulator (rad/s) is defined as $\omega_z = k_i/k_p$. The proportional gain of the PI voltage regulator is computed to impose a specific crossover frequency ω_{cv} of the voltage loop. The resulting regulator gains are provided by the following equation:

$$\begin{aligned} k_p &= \frac{\omega_{cv}^2 C \cdot (1+\omega_{cv}^2 \tau_I^2)}{\sqrt{(\omega_z+\omega_{cv}^2\tau_I)^2+(\omega_{cv}-\omega_{cv}\omega_z\tau_I)^2}} \\ k_i &= k_p \cdot \omega_z. \end{aligned} \tag{7}$$

A factor plays a role in the loop shaping of the PI controller and the overall stability of the control. This factor is the output capacitance *C*. Due to the production tolerances, the aging of the components, and the voltage bias, the capacitance of the output capacitors may deviate from its nominal value. Its effects reflect mainly on the voltage control loop. A variation of the real capacitance *C* with respect to the nominal one leads to an effective change of the voltage control loop bandwidth H_v. The study in Fig. 7 shows the closed-loop transfer function, obtained under the assumption of Fig. 6. As it is noted, the closed-loop crossing, phase margin, and gain are affected by the capacitor inequalities. It is noted that owing to the margin used when sizing the voltage control loop bandwidth, the control is still stable, even if underdamped in the worst-case scenario of Fig. 8 (i.e., a capacitance variation of ± 40%).

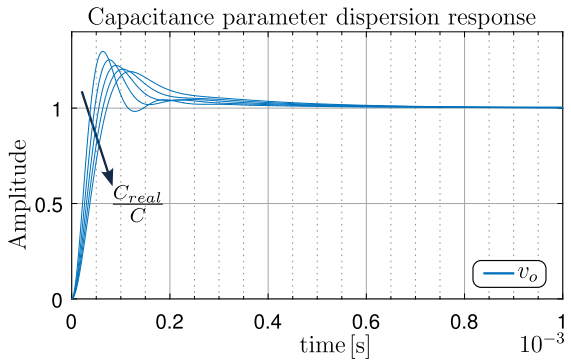


FIGURE 8. Capacitor parameter drift influence on voltage loop step response.

B. DEADBEAT CURRENT CONTROL

The main contribution of this article consists of the deadbeat current control, whose high dynamic performances allow obtaining a high regulation bandwidth of the outer voltage control. The proposed deadbeat current control computes the inductor reference voltage $v^*_{L,abc}$ based on the difference between the inductor's reference current $i^*_{L,abc}$ and the corresponding predicted value $i^{[k]}_{L,abc}$, derived from the measured value $i^{[k-1]}_{L,abc}$. The reference voltages $v^*_{L,abc}$ obtained by the deadbeat current control are then converted into the corresponding duty cycles using the "democratic modulator." This way, the switching losses of the converter are minimized, since for each phase only one switching cell is commutated [3]. According to the deadbeat operation, the prediction of the inductor's current $i^{[k]}_{L,abc}$ is performed by implementing the discrete-time representation of the state-space model in (4).

Considering one phase of the Y-inverter, the corresponding discrete-time equations are computed, as shown in the following equation, where the generic phase is denoted with the subscript $x = \{a, b, c\}$:

$$\begin{bmatrix} I^{[k]}_{L,x} \\ V^{[k]}_{o,x} \end{bmatrix} = A_d \cdot \begin{bmatrix} I^{[k-1]}_{L,x} \\ V^{[k-1]}_{o,x} \end{bmatrix} + B_d \cdot \begin{bmatrix} V^{[k-1]}_{IN,x} \\ I^{[k-1]}_{o,x} \end{bmatrix}. \tag{8}$$

In (8), the superscript $[k-1]$ denotes the measured phase quantities of inductors current $I_{L,x}$, output capacitor voltage $V_{o,x}$, DC voltage $V_{IN,x}$, and motor current $I_{o,x}$. The discrete-time matrices A_d and B_d are computed using the well-known transformations available in the literature, hereafter reported for convenience

$$A_d = e^{A \cdot T_s} \tag{9}$$

$$B_d = (A_d - I) \cdot A^{-1} \cdot B. \tag{10}$$

After performing several mathematical manipulations, (9) and (10) are computed as follows:

$$A_d = \begin{bmatrix} \cos\left(\frac{T_s \cdot d_2}{\sqrt{LC}}\right) & -\sqrt{\frac{C}{L}} \cdot \sin\left(\frac{T_s \cdot d_2}{\sqrt{LC}}\right) \\ \sqrt{\frac{L}{C}} \cdot \sin\left(\frac{T_s \cdot d_2}{\sqrt{LC}}\right) & \cos\left(\frac{T_s \cdot d_2}{\sqrt{LC}}\right) \end{bmatrix} \tag{11}$$

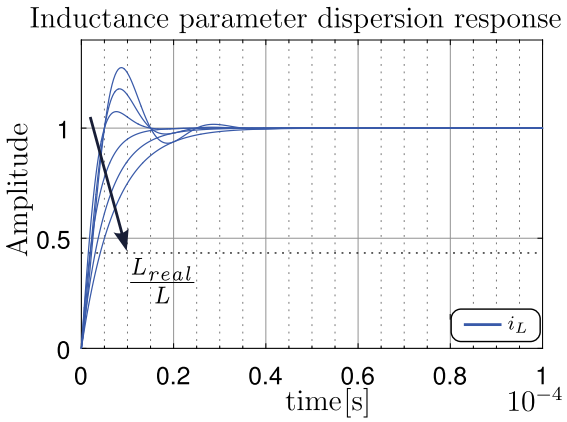


FIGURE 9. Current step response to real inductance value dispersion.

$$B_d = \begin{bmatrix} \frac{d_1}{d_2} \cdot \sqrt{\frac{C}{L}} \cdot \sin\left(\frac{T_s \cdot d_2}{\sqrt{LC}}\right) & \left(1 - \cos\left(\frac{T_s \cdot d_2}{\sqrt{LC}}\right)\right) \cdot \frac{1}{d_2} \\ \left(1 - \cos\left(\frac{T_s \cdot d_2}{\sqrt{LC}}\right)\right) \cdot \frac{d_1}{d_2} & -\frac{1}{d_2} \cdot \sqrt{\frac{L}{C}} \cdot \sin\left(\frac{T_s \cdot d_2}{\sqrt{LC}}\right) \end{bmatrix}. \tag{12}$$

As previously mentioned, the deadbeat current control exhibits a two-step delay between reference update and signal actuation. However, it offers the advantage of the fastest possible response between applying the control signal and reaching the desired output [27]. In other words, the proposed deadbeat current controller for the Y-inverter yields the best possible dynamic performance while employing PWM, given the switching frequency, as demonstrated by the experimental results.

The inductor L and the capacitor C in this analysis have been assumed to be ideal. However, the real-world components deviate from their nominal values, and on top of that, the inductance decreases at high flux values due to saturation. The inductor L is the most important parameter affecting the control response because it directly influences the current-control loop, this is because it is the main parameter that influences the current control loop onto which the deadbeat acts. This is why a sensitivity analysis was done on the deadbeat current control response over a variation of the inductance in Fig. 9.

The analysis carries out a per-unit (p.u.) step response by varying the real converter inductance L, in the figure called L_{real}, from a value of 0.8 to 1.2 p.u. It is important to note that 0.5 p.u. constitutes the instability limit of the system. The effect of inductance value dispersion can be categorized as a variation in the damping of a second-order dynamic system. Similarly to parametric dispersion, core saturation changes the inductance value of the inductor L. However, this value is more easily predicted and shall be taken into account to properly tune the deadbeat current control.

While capacitors, as aforementioned in Section III-A, vary their capacitance over voltage bias and age, the effect on the inductor current I_L, determined by the first rows of A and B (4), is of negligible importance.

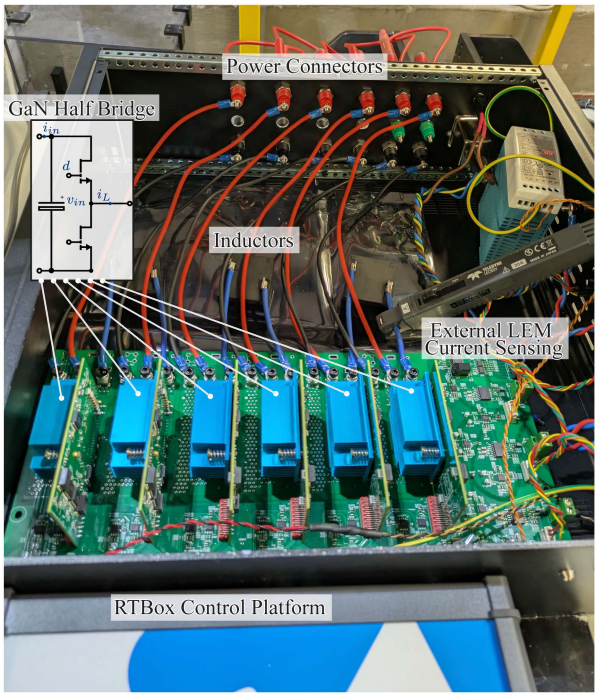


FIGURE 10. View of the Y-inverter prototype.

TABLE 1. Y-Inverter Main Parameters

DC-Link	V_{DC}	240	V
Max Output Voltage	$V_{o,max}$	300	V
Max Output Current	$I_{o,max}$	25	A
Switching frequency	f_{sw}	100	kHz
DC-Link	C_{DC}	33	µF
Inductance	L	50	µH
Output Capacitance	C	11	µF

IV. EXPERIMENTAL RESULTS

The experimental verification has been performed using a reduced-scale Y-inverter prototype rated 12 kVA, shown in Fig. 10. It has a modular structure and comprises six switching cells built with Texas Instruments LMG3526R030 GaN transistors. These switches incorporate integrated gate drivers, junction temperature sensing, overtemperature, and overcurrent protection. Other salient data of chosen GaN transistors include on-state resistance of 26 mω at room temperature and blocking voltage of 650 V. The Y-inverter main parameters are summarized in Table 1.

The digital control of the Y-inverter has been implemented using the Plexim RTBox2 platform [30], using synchronized switching and sampling frequencies of 100 kHz. Particular attention must be paid to PWM synchronization with ADC sampling instances; a single carrier was adopted to synchronize PWM pulses, interrupt service routines, and ADC samplings. The Y-inverter is equipped with a position sensor interface utilized for torque control.

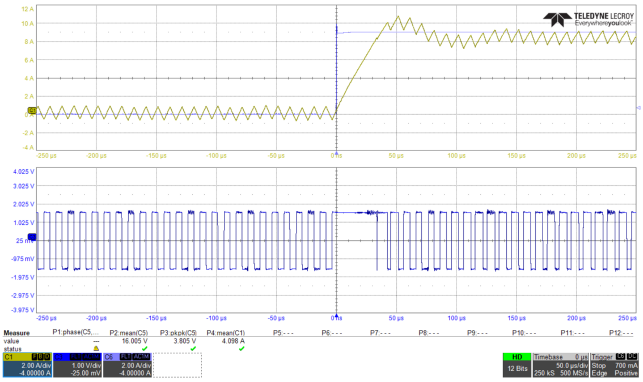


FIGURE 11. Deadbeat current control reference change response. Top: reference and measured current (2 A/div); bottom: upper switch PWM signal of the buck switching cell (1 V/div).

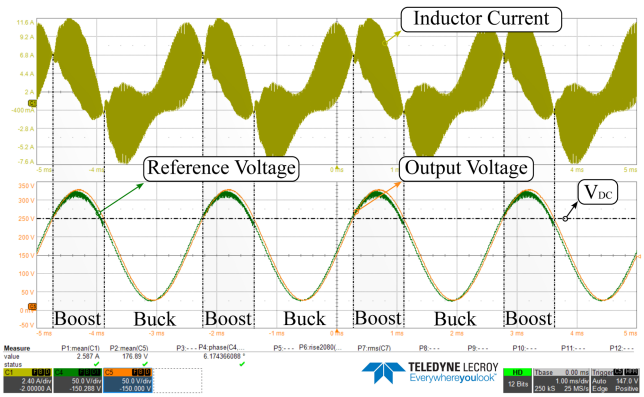


FIGURE 12. Voltage control response with sinusoidal excitation of 400 Hz. Top: inductor current i_L (2.4 A/div); bottom: reference v_o^* and output v_o voltages (50 V/div).

In final implementations, the control shall be implemented using standard embedded platforms, such as automotive microcontrollers. To lighten the computational burden, the voltage control loop and the motor control loop can be decoupled in frequency, running only the lighter voltage control algorithm at the higher sampling frequency and the motor control at a lower frequency, around the ones used in typical motor control. To validate this assumption, the motor control of the motor-control test in Section IV-D was carried out with a motor control update frequency of 20 kHz, more than enough to satisfy standard motor control algorithms.

The deadbeat control requires a PI control, frame rotations, and A_d and B_d matrix updates. Although, thanks to the coordinate rotation digital computer algorithm and special attention to the implementation, it is feasible to achieve frequencies upward of 100 kHz necessary for the control on high-end automotive microcontrollers, which employ clock frequencies from 100 to 600 MHz. The execution of the control described was implemented on an industrial ARM Cortex M4, with a clock of 200 MHz. The execution time was measured as 5.5 μs.

The experimental work included the following tests.

A. Verification of the current control response.
B. Single-phase operation.
C. Three-phase operation with resistive load.
D. Three-phase operation with torque control

A. VERIFICATION OF THE CURRENT CONTROL RESPONSE

While operating a single-phase PEBB unit in current control, a significant step change of the inductor current reference from 0 to 9 A is imposed, obtaining the inductor current i_L control response shown in Fig. 11. It is noted the deadbeat response of the inductor current is characterized by the minimum rising time and very negligible overshoot, although the duty cycle of the switching cell is saturated to its maximum value, as confirmed by the corresponding PWM signal shown in Fig. 11. However, a small steady-state error is reported. This is due to the current prediction error when implementing (8), which is affected by the accuracy in estimating the parameters of inductance L, capacitance C, and effective duty cycle d_2 due to deadtime distortion.

Nevertheless, it is highlighted that the steady-state error has negligible impact in practice, since the outer voltage PI regulator automatically compensates it, thus guaranteeing zero steady-state error in the voltage control loop.

B. SINGLE-PHASE OPERATION

The single-phase operation has been tested by still operating one single-phase PEBB unit, whose voltage reference for the voltage control has been imposed on a sinusoidal signal. Two tests have been performed as follows.

In the first test, a 400-Hz sinusoidal voltage reference has been imposed with a DC bias of 175 V and a peak-to-peak amplitude of 300 V. The experimental results, as shown in Fig. 12, demonstrate a very good tracking of the sinusoidal voltage reference. Moreover, the different operating modes, i.e., buck and boost modes, are clearly marked. Since a PI regulator with a sinusoidal voltage reference is implemented, a phase delay of 6.17° is reported between the reference voltage and the output voltage. Nevertheless, this delay is not present in three-phase operation, as it is canceled by the $dq\gamma$ transformation implemented in the proposed architecture, as shown in Fig. 4.

In the second test, the frequency of the reference voltage has been increased tenfold, to 4 kHz, obtaining the results shown in Fig. 13. It is noted an expected greater delay compared to the first test, including the discretization distortion introduced by the sampling frequency of the digital controller. Nonetheless, the phase delay remains below 28.9°, demonstrating that the bandwidth of the voltage control is much higher than 4 kHz, although sampling and switching frequencies are 100 kHz, i.e., only 25 times higher. This significant result is due to the ultra high bandwidth of the inner deadbeat current control, without which it would not have been possible.

The voltage quality is further assessed in Figs. 14 and 15, showing the frequency analysis of the output voltage

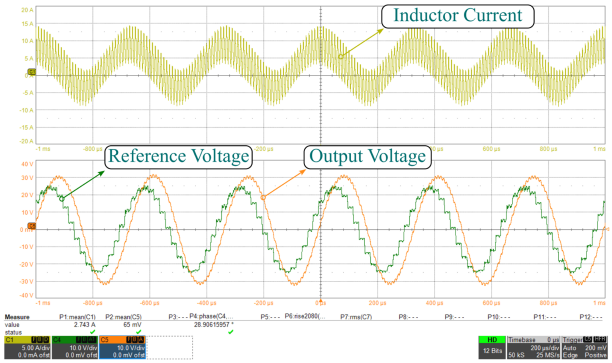


FIGURE 13. Voltage control response with sinusoidal excitation of 4 kHz. Top: inductor current i_L (5 A/div); bottom: reference v_o^* and output v_o voltages (10 V/div).

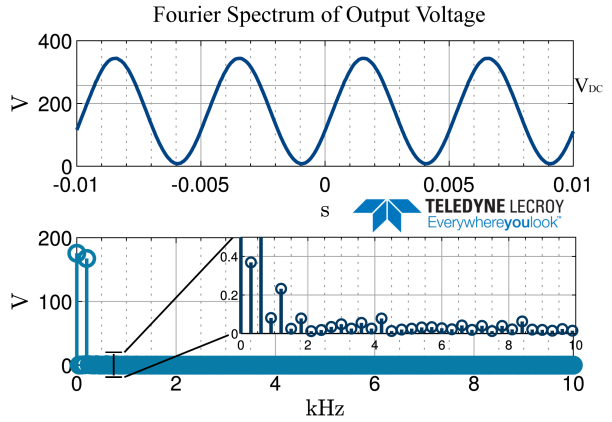


FIGURE 14. Voltage control response with sinusoidal excitation of 200 Hz: frequency analysis of the output voltage.

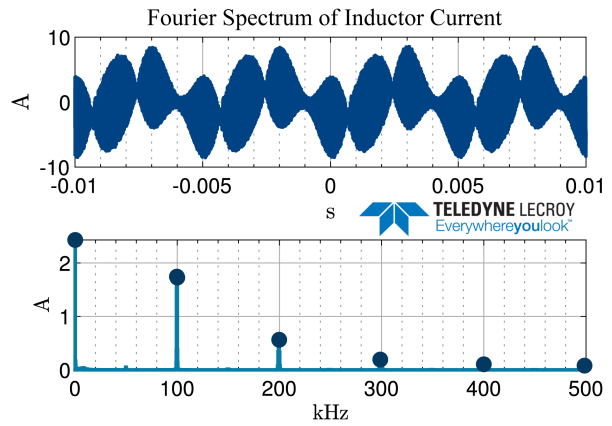


FIGURE 15. Voltage control response with sinusoidal excitation of 200 Hz: frequency analysis of the inductor current.

while imposing a DC bias of 175 V, a peak-to-peak amplitude of 340 V, and a frequency of 200 Hz. From Fig. 14, a near-sinusoidal waveform quality is noted, with very low distortion. The frequency analysis of the inductor current is instead shown in Fig. 15, highlighting a null DC component since no load conditions have been tested. Moreover, the fundamental component at 200 Hz is reported, together with

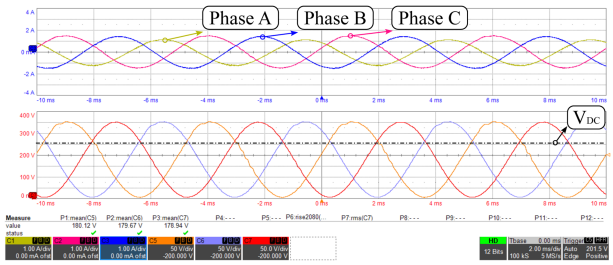


FIGURE 16. Three-phase voltage control with resistive load. Top: output currents $i_{o,abc}$ (1 A/div); bottom: output voltages $v_{o,abc}$ (50 V/div).

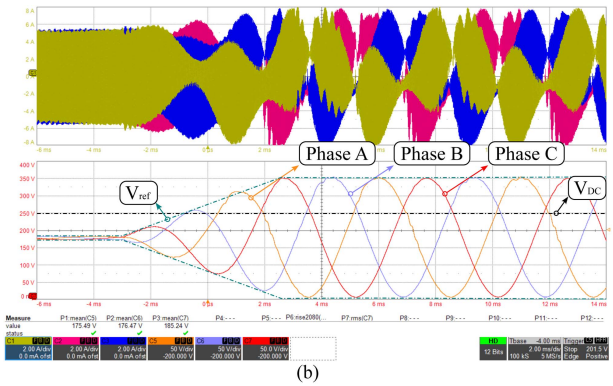


FIGURE 17. Three-phase voltage control with resistive load and variable voltage amplitude. Top: inductors current $i_{L,abc}$ (2 A/div); bottom: output voltages $v_{o,abc}$ (50 V/div).

the harmonic components having a frequency close to the switching one and its multiples.

C. THREE-PHASE OPERATION WITH RESISTIVE LOAD

The three-phase operation has been preliminarily implemented with three PEBB units supplying a 160 W three-phase resistive load. In detail, a 200-Hz sinusoidal voltage reference has been imposed with a DC bias of 175 V and a peak-to-peak amplitude of 350 V. The experimental results for steady-state operation are shown in Fig. 16.

As expected, the load currents exhibited no homopolar component since the three-phase resistive load is star-connected with an isolated midpoint. However, a DC component is observed in the load currents, resulting from offset discrepancies in the voltage sensors and inequalities in the load resistors. Obviously, this distorted component can be easily canceled when the output currents are closed-loop controlled.

Finally, the smooth voltage regulation response is demonstrated in Fig. 17, showing a variable peak-to-peak amplitude of the reference voltages from 10 to 350 V with a slope of 25 kV/s.

D. THREE-PHASE OPERATION WITH TORQUE CONTROL

A further contribution of this article consists of validating the proposed voltage control by using the Y-inverter prototype to supply a torque-controlled IPM motor; this is typical for traction application drives. The motor used for the tests is

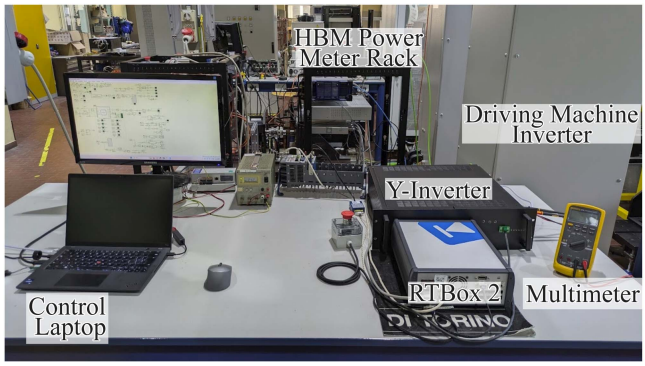


FIGURE 18. Experimental setup of the Y-inverter-based electric drive.

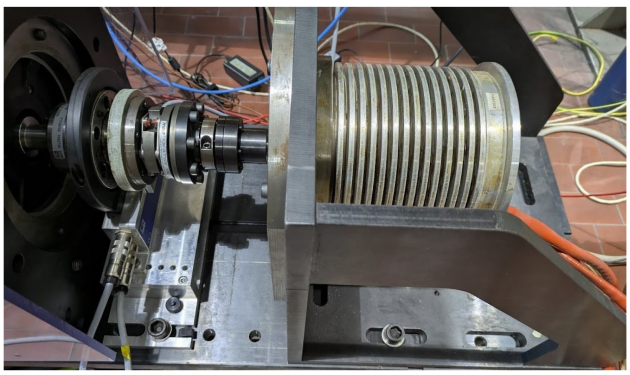


FIGURE 19. View of the IPM machine under test (right), torque meter (middle), and DM (left).

specifically designed for light traction applications. Technically, the control and hardware frequencies of the converter can be sized regardless of the drive train power. However, since switching losses do not scale linearly, it is common to have reduced switching frequencies at higher converter powers. However, thanks to the superior properties of GaN with respect to traditional IGBT and MOSFET drives, it is possible to achieve comparable switching frequencies at converter sizes of around 100 kW, suiting small car applications [31]. Higher power converters can allow for higher inductor L current ripple; however, to keep the overall stability, it is necessary to keep the LC product constant in order to behave in similar ways regardless of the inductor L magnitude with respect to control performances. The Y-inverter is shown in Fig. 18, while the IPM motor is shown in Fig. 19. The IPM motor is coupled to a speed-controlled driving machine (DM) via the torque meter HBK T40B. This way, the torque accuracy obtained by using the proposed voltage-controlled Y-inverter has been validated. The IPM machine parameters are reported in Table 2. All the electrical (voltages and currents) and mechanical (torque and position) measurements have been collected using the data recorder HBM GEN4tB tethered mainframe, adopting high-voltage and high-sampling data acquisition cards HBM GN311B.

The eMotor control has been implemented with the control architecture shown in Fig. 3. The adopted torque controller

TABLE 2. Main Parameters of the IPM Under Test

Maximum torque	T_{max}	16	Nm
Maximum speed	ω_{max}	5000	r/min
Pole pairs	pp	2	
Stator resistance	R	75	mΩ
PM flux	λ_m	101	mVs
d-axis rated inductance	L_d	12	mH
q-axis rated inductance	L_q	72	mH

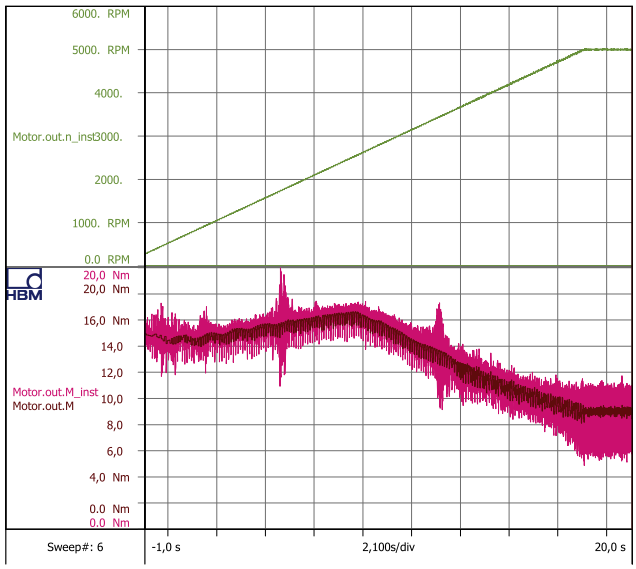


FIGURE 20. MTPS results. From top to bottom: measured speed; measured instantaneous and averaged torques.

is the flux polar control (FPC), whose details are reported in [32]. It is underlined that any torque control solution for IPM drives can be adopted, so the schematic block from Fig. 3 has a high degree of generality.

The performance of the proposed voltage control in regulating the IPM motor torque has been validated through the following experimental tests.

1) Section IV-D1) Maximum torque per speed (MTPS).
2) Section IV-D2) Torque reversals during dynamic speed conditions.

1) MAXIMUM TORQUE PER SPEED

The MTPS test finds the maximum torque capability of the motor for the entire speed range. According to Table 2, the DM imposes the speed from zero up to the maximum limit of 5000 r/min, while the motor under test (MUT) is torque-controlled at its maximum torque of 16 N·m.

The MTPS test results collected by the data recorder and shown in Figs. 20 and 21, considering an amplitude limit of the phase currents of 25 A (see Table 1). This current limit is above the one necessary for the maximum torque request of 16 N·m. In parallel, the peak-to-peak amplitude of the inverter output voltages has been limited to 270 V, while the DC bias of the Y-inverter output voltages has been set to 150 V.

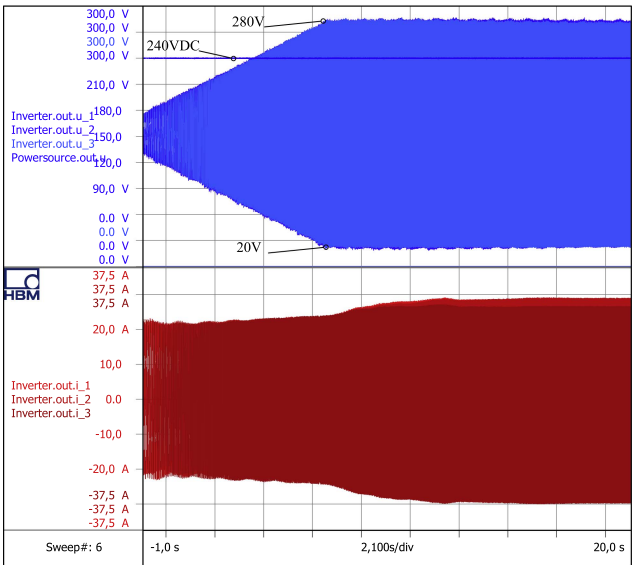


FIGURE 21. MTPS results. From top to bottom: measured inverter output voltages and DC input voltage; measured inverter output currents.

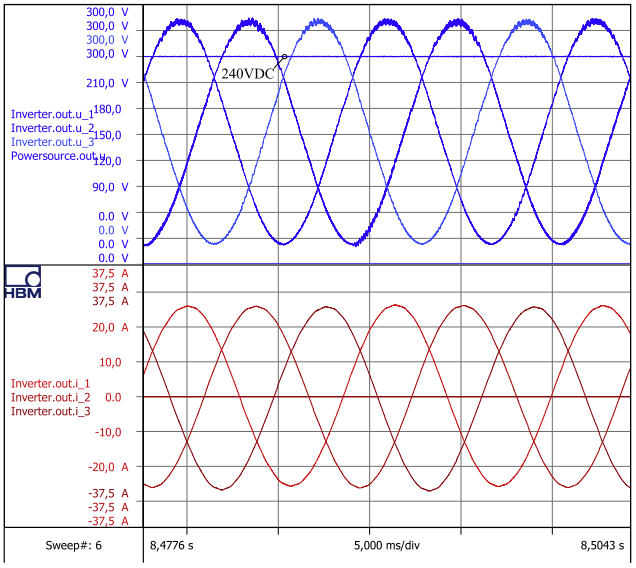


FIGURE 22. Magnification of MTPS results from Fig. 21. From top to bottom: measured inverter output voltages and DC input voltage; measured inverter output currents.

The speed and torque during the MTPS test are shown in Fig. 20. It is noted the maximum torque per ampere (MTPA) operation at low speed, followed by the flux weakening (FW) one from the base speed of 2600 r/min.

From Fig. 21, a small torque error is reported in the MTPA operation at low speed. This error is due to the phase currents measurement that has been performed using current transducers affected by offset introduced by electromagnetic interference. The observed measurement error is primarily attributed to hardware limitations. While the system incorporates three built-in current sensors, the control algorithm necessitates the measurement of both motor and inductor currents. Consequently, an external current sensing board was employed for motor current acquisition. However, these measurements are more susceptible to noise and offset due to increased exposure to electrical disturbances, as well as grounding reference discrepancies between the external sensing circuitry and the main system. However, it is noted that this torque error is progressively canceled by increasing the speed due to the adopted FPC torque controller [32]. Indeed, the FPC performs torque regulation by directly controlling the stator flux vector of the machine, whose estimate is provided by a Gopinath-style flux observer [32]. In the medium- and high-speed range, this observer performs the stator flux estimation by integrating the machine's electromotive forces, thus resulting in immunity to the phase current measurements.

Since the inverter input DC-link voltage is 240 V, the buck and boost cells within the PEBB units are activated based on the corresponding inverter's output voltage. This can be noted in Fig. 22, which provides a detailed view (two periods of fundamental frequency) of the instantaneous inverter output voltages along with the input DC link voltage (upper plot). When the instantaneous phase output voltage is higher than

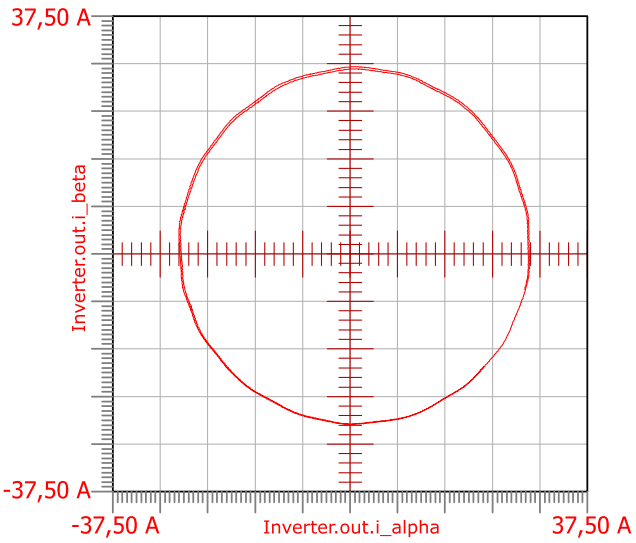


FIGURE 23. Trajectory of the steady-state stator current space vector in stationary $\alpha\beta$ coordinates along the MTPS profile.

the input DC link voltage, the phase PEBB operates in boost mode; otherwise, the buck mode is performed.

Still considering Fig. 21, it is noted that the output current amplitudes increase starting from the base speed. This is justified since below the base speed, the torque limit of the MUT must be satisfied, resulting in stator current amplitude lower than the Y-inverter limit (25 A). When the FW operation starts, the torque controller increases the stator current amplitude up to the Y-inverter limit to keep the torque as high as possible while reducing the stator flux amplitude.

As it can be clearly noted in Fig. 22, the inverter output voltages are practically sinusoidal with identical DC bias (150 V),

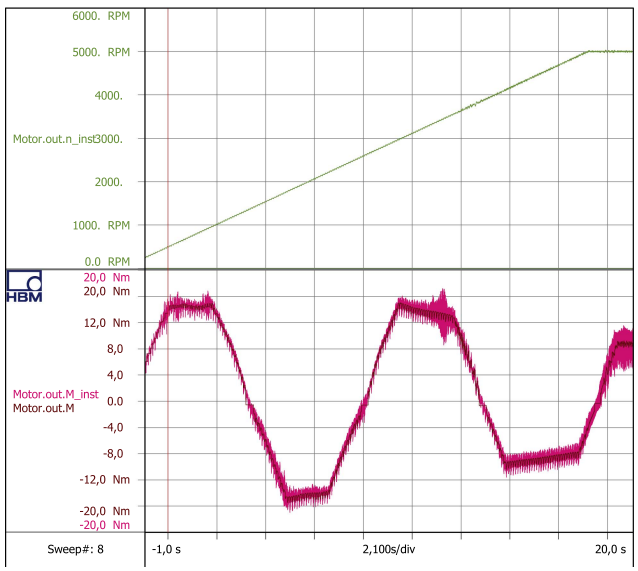


FIGURE 24. Torque reversals test result. From top to bottom: measured speed; measured instantaneous and averaged torques.

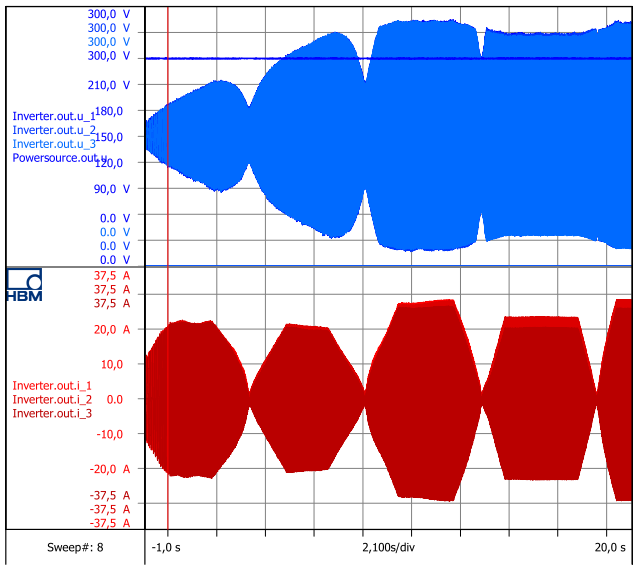


FIGURE 25. Torque reversals test results. From top to bottom: measured inverter output voltages and DC input voltage; measured inverter output currents.

thus eliminating any aging on the motor windings and leakage currents due to the dv/dt effects. As also shown in Fig. 22 (bottom plot), the motor currents are near sinusoidal as well, so no additional PWM-induced losses are produced in the MUT. The motor currents are well-balanced, as demonstrated in Fig. 23, which shows the circular trajectory of the stator current space vector in the stationary $\alpha\beta$ frame. A small DC component can be observed due to the previously mentioned offset in the phase currents measurement.

A summary of the most significant quantities is listed in the following paragraph. It is noted that, since the article deals with the control algorithm of the converter and not strictly about the design, these values are reported as an indication of performance and not necessarily a benchmark. The measurement point is set at the speed of 5000 r/min, with a torque of 11.5 N·m, corresponding to the maximum speed and torque point of Fig. 20. The AC quantities are 24.5 A and 180 V as peak values. The total harmonic distortions are 1.00% and 1.46%, respectively, for current and voltage. The inverter, motor, and whole drive efficiencies are, respectively, 97.5%, 93.3% and 91%. The torque is characterized by oscillations with a standard deviation of 1.2 N·m.

2) TORQUE REVERSALS DURING SPEED DYNAMIC CONDITIONS

This test verifies the torque control dynamic performance of torque regulation and its stability for maximum torque production from standstill to the maximum operating speed. In detail, the torque reference is reversed from motoring to generation and vice versa along the MTPS profile. The frequency of torque reversals has been set to 0.1 Hz to emphasize the dynamic torque accuracy while the speed significantly changes. The obtained results are shown in Fig. 24. It is noted that the torque is properly reversed without reporting any underdamping or instability issue starting from the MTPA operation at low speed up to the deep FW at the maximum speed.

The measured voltages and currents while executing this test are reported in Fig. 25. When the torque is close to zero, also the stator currents tend to be null. This behavior is justified since the MUT is an IPM motor belonging to PM-assisted synchronous reluctance typology. Therefore, most of the torque is produced by the machine's saliency rather than permanent magnets, whose contribution to the stator flux linkage is small.

From Fig. 25, it is evident how the peak-to-peak voltages in motoring are a bit higher than those in generation due to the effects of stator resistance and iron losses. Also, it is still an increase of stator current amplitude in FW operation up to the Y-inverter limit to keep the torque as high as possible in terms of absolute values. Consequently, the asymmetries between the stator currents due to the offset of the corresponding transducer are emphasized. The accurate compensation of these offsets is not critical when using flux-based torque controllers, such as the FPC. However, this aspect becomes critical when implementing torque controllers based on the current vector control. This issue requires more investigation and represents a future development of this work. In summary, Fig. 25 clearly demonstrates how output currents and voltages are perfectly regulated without reporting any uncontrollability issue, such as spikes or oscillations.

V. CONCLUSION

This article proposed an advanced voltage control of GaN-based Y-inverters for torque-controlled traction applications. The proposed solution brings in added value by implementing the accurate deadbeat control of the Y-inverter inductors

current, thus allowing very high regulation bandwidth of the voltage control. This way, using Y-inverters in motor drives for traction, which adopt high performance torque controllers becomes possible, representing a novelty in the literature on potential applications of such converter typologies.

The accurate computation of the discrete-time model of the Y-inverter PEBB has been reported, allowing to implement a deadbeat control of the Y-inverter inductor currents featuring ultra-high dynamic performance without exhibiting uncontrollability and significant steady-state errors. The outer three-phase voltage control of the Y-inverter is implemented in rotating coordinates to guarantee zero error in AC conditions by simply using conventional PI regulators, representing a further feature of the proposed solution compared to the existing literature contributions. Moreover, an accurate tuning procedure of this PI voltage regulator was reported, achieving an analytical voltage loop bandwidth of 6 kHz with a sampling frequency of 100 kHz.

The proposed voltage control has been validated on a reduced-scale GaN-based Y-inverter prototype supplying a torque-controlled IPM motor for light traction applications, obtaining voltages and currents with a THD below 1.5%. The experimental results demonstrated how the proposed voltage control can be combined with advanced torque controllers for traction, guaranteeing maximum torque production along wide speed range and accurate torque controllability in steady-state and dynamic conditions, including both motoring and generator operation of the machine. Finally, it is highlighted how the Y-inverter provides a near-sinusoidal voltage supply to the electric motor, leveraging the advantages of GaN technology to achieve high switching frequency. The sinusoidal voltage supply eliminates issues associated with the PWM supply, such as stator winding aging, electrically induced bearing damage, PWM-induced losses, partial-discharge inception voltages, and the need for magnet segmentation.

Future development of this work includes exploiting the DC bias of the Y-inverter output voltages to extend the voltage regulation range. Also, the potential advantage of parallelizing more Y-inverter PEBBs will be investigated, allowing the adoption of this converter typology in high-power motor drives.

REFERENCES

[1] J. G. Kassakian and T. M. Jahns, "Evolving and emerging applications of power electronics in systems," *IEEE Trans. Emerg. Sel. Topics Power Electron.*, vol. 1, no. 2, pp. 47–58, Jun. 2013.

[2] G. Deboy, O. Haeberlen, and M. Treu, "Perspective of loss mechanisms for silicon and wide band-gap power devices," *CPSS Trans. Power Electron. Appl.*, vol. 2, no. 2, pp. 89–100, 2017.

[3] M. Antivachis, D. Bortis, L. Schrittwieser, and J. W. Kolar, "Three-phase buck-boost Y-inverter with wide DC input voltage range," in *Proc. 2018 IEEE Appl. Power Electron. Conf. Expo.*, Mar. 2018, pp. 1492–1499.

[4] M. Antivachis, D. Bortis, D. Menzi, and J. W. Kolar, "Comparative evaluation of Y-inverter against three-phase two-stage buck-boost DC-AC converter systems," in *Proc. 2018 Int. Power Electron. Conf.*, May 2018, pp. 181–189.

[5] A. Y. Farag, T. Younis, P. Mattavelli, and D. Biadene, "AC grid-interface bidirectional buck-type converters for DC microgrids: A comparative study," in *Proc. 48th Annu. Conf. IEEE Ind. Electron. Soc.*, Oct. 2022, pp. 1–6.

[6] A. Y. Farag, D. Biadene, P. Mattavelli, and T. Younis, "Three-phase four-wire bidirectional Y-converter for an enhanced interface between the AC grid and the unipolar DC microgrid," in *Proc. 8th IEEE Workshop Electron. Grid*, Oct. 2023, pp. 1–6.

[7] A. Y. Farag, D. Biadene, T. Caldognetto, and P. Mattavelli, "Multiport Y-converter for three-phase AC grid integration with DC systems," in *Proc. 2024 IEEE 15th Int. Symp. Power Electron. Distrib. Gener. Syst.*, Jun. 2024, pp. 1–6.

[8] M. Antivachis, J. A. Anderson, D. Bortis, and J. W. Kolar, "Analysis of a synergetically controlled two-stage three-phase DC/AC buck-boost converter," *CPSS Trans. Power Electron. Appl.*, vol. 5, no. 1, pp. 34–53, Mar. 2020.

[9] M. Antivachis, N. Kleynhans, and J. W. Kolar, "Three-phase sinusoidal output buck-boost GaN Y-inverter for advanced variable speed AC drives," *IEEE Trans. Emerg. Sel. Topics Power Electron.*, vol. 10, no. 3, pp. 3459–3476, Jun. 2022.

[10] S. Waffler and J. W. Kolar, "A novel low-loss modulation strategy for high-power bidirectional buck BM boost converters," *IEEE Trans. Power Electron.*, vol. 24, no. 6, pp. 1589–1599, Jun. 2009.

[11] P. Gautam, Y. Lee, R. Takahashi, and A. Castellazzi, "A study of pulse density modulation to GaN Y-inverter," in *Proc. 2024 IEEE 10th Int. Power Electron. Motion Control Conf.*, May 2024, pp. 4498–4503.

[12] Y. Lee, A. Castellazzi, S. Domae, and T. Nakamura, "Regenerative Halbach-motor traction drive powered by an active-damping controlled interleaved Y-inverter," in *Proc. IEEE 10th Int. Power Electron. Motion Control Conf.*, May 2024, pp. 4194–4199.

[13] Y. Endo, M. Minami, H. J. Jaber, and A. Castellazzi, "Experimental study of interleaved Y-inverter performance," in *Proc. 24th Eur. Conf. Power Electron. Appl.*, Sep. 2022, pp. 1–8.

[14] X. Chen, D. Xu, F. Liu, and J. Zhang, "A novel inverter-output passive filter for reducing both differential- and common-mode dv/dt at the motor terminals in PWM drive systems," *IEEE Trans. Ind. Electron.*, vol. 54, no. 1, pp. 419–426, Feb. 2007.

[15] D. Menzi, L. Kappeler, P. Ziegler, D. Biadene, and J. W. Kolar, "Wide DC output voltage range buck-boost 6-Module Y-rectifier featuring full power delivery in 3-Phase and 1-Phase operation," *IEEE Access*, vol. 12, pp. 189804–189819, 2024.

[16] K. Shirabe et al., "Advantages of high frequency PWM in AC motor drive applications," in *Proc. IEEE Energy Convers. Congr. Expo.*, Sep. 2012, pp. 2977–2984.

[17] D. Cittanti, E. Vico, E. Armando, and R. Bojoi, "Analysis and conceptualization of a 800 v 100 kVA Full-GaN three-level flying capacitor inverter for next-generation electric vehicle drives," in *Proc. 2022 Int. Power Electron. Conf.*, May 2022, pp. 2320–2327.

[18] D. Menzi, L. Imperiali, E. Bürgisser, M. Ulmer, J. Huber, and J. W. Kolar, "Ultra-lightweight high-efficiency buck-boost DC-DC converters for future eVTOL aircraft with hybrid power supply," *IEEE Trans. Transport. Electrific.*, vol. 10, no. 4, pp. 10297–10313, Dec. 2024.

[19] M. Rashid, *Power Electron.: Circuits, Devices, and Appl.*. Hoboken, NJ, USA: Pearson/Prentice Hall, 2004. [Online]. Available: https://books.google.it/books?id=YH0eAQAAIAAJ

[20] E. A. Jones, F. F. Wang, and D. Costinett, "Review of commercial GaN power devices and GaN-Based converter design challenges," *IEEE Trans. Emerg. Sel. Topics Power Electron.*, vol. 4, no. 3, pp. 707–719, Sep. 2016.

[21] A. Udabe, I. Baraia-Etxaburu, and D. G. Diez, "Gallium nitride power devices: A state of the art review," *IEEE Access*, vol. 11, pp. 48628–48650, 2023.

[22] E. A. Jones et al., "Characterization of an enhancement-mode 650-V GaN HFET," in *Proc. 2015 IEEE Energy Convers. Congr. Expo.*, Sep. 2015, pp. 400–407.

[23] N. Keshmiri, D. Wang, B. Agrawal, R. Hou, and A. Emadi, "Current status and future trends of GaN HEMTs in electrified transportation," *IEEE Access*, vol. 8, pp. 70553–70571, 2020.

[24] M. Rahman, A. Chiba, and T. Fukao, "Super high speed electrical machines - summary," in *Proc. IEEE Power Eng. Soc. Gen. Meeting*, Jun. 2004, pp. 1272–1275.

[25] H. N. Tran, A. Castellazzi, S. Domae, T. Dong, and T. Nakamura, "Low-voltage-battery powered hybrid-GaN/SiC Y-inverter dual-rotor Halbach motor drive for light electric vehicles," in *Proc. 24th Int. Conf. Elect. Machines Syst.*. Gyeongju, South Korea, Oct. 2021, pp. 699–704.
[26] F. Campanelli, F. Mandrile, S. Rubino, E. Armando, and R. Bojoi, "Deadbeat control of three-phase sinusoidal output Y-inverter for automotive powertrains," in *Proc. 2024 IEEE Energy Convers. Congr. Expo.*, Oct. 2024, pp. 4457–4463.
[27] S. Buso and P. Mattavelli, *Digital Control in Power Electronics, Ser. Lectures on Power Electronics*. San Rafael, CA, USA: Morgan & Claypool Publishers, 2006.
[28] S. Rubino, L. Tolosano, and R. Bojoi, "Direct flux control: A viable torque control approach for three-phase and multi-phase motor drives for transportation electrification," in *Proc. IEEE Workshop Elect. Machines Des.*, Apr. 2025, pp. 1–10.
[29] T. Sakharuk, B. Lehman, A. Stankovic, and G. Tadmor, "Effects of finite switching frequency and delay on PWM controlled systems," *IEEE Trans. Circuits Syst. I: Fundam. Theory Appl.*, vol. 47, no. 4, pp. 555–567, Apr. 2000.
[30] RT Box 2 Plexim, (n.d.). [Online]. Available: https://www.plexim.com/products/rt_box/rt_box_2
[31] S. Giuffrida, F. Mandrile, and R. Bojoi, "Topology comparison of GaN-Based sine-wave inverters for 400 V electrified vehicles," in *Proc. IEEE Energy Convers. Conf. Congr. Expo.*. Philadelphia, PA, USA, Oct. 2025, pp. 1–8.
[32] S. Rubino, L. Tolosano, F. Mandrile, E. Armando, and R. Bojoi, "Flux polar control (FPC): A unified torque controller for AC motor drives," *IEEE Trans. Ind. Appl.*, vol. 59, no. 4, pp. 4140–4163, Jul. 2023.



FEDERICO CAMPANELLI (Student Member, IEEE) received the B.Sc. and M.Sc. degrees in mechanical and electrical engineering from Politecnico di Torino, Torino, Italy, in 2018 and 2023, respectively, where he is currently working toward the Ph.D. degree in electrical engineering.

He is part of the power electronics innovation center. His research interests include control and design of wide band-gap based power converters and their applications to electric drive trains.



FABIO MANDRILE (Member, IEEE) received the M.Sc. and Ph.D. degrees in electrical engineering from Politecnico di Torino, Torino, Italy, in 2017 and 2021, respectively.

His research interests include virtual synchronous generators, power electronics for grid-connected applications, and the experimental characterization of converters and motor drives.



SANDRO RUBINO (Senior Member, IEEE) received the M.Sc. and Ph.D. degrees in electrical engineering from Politecnico di Torino, Torino, Italy, in 2014 and 2019, respectively.

He is currently an Associate Professor with the Energy Department "G. Ferraris," Politecnico di Torino. His research interests include modeling and controlling multiphase electrical machines and high-performance motor drives.

Prof. Rubino is currently the Secretary of the Industrial Drive Committee (IDC) of the IEEE Industry Applications Society (IAS). He is an Associate Editor for IEEE TRANSACTIONS ON INDUSTRY APPLICATIONS and IEEE JOURNAL OF EMERGING AND SELECTED TOPICS IN POWER ELECTRONICS. He was the recipient of the four paper awards from IAS-IDC and two Ph.D. thesis awards for the design and validation of advanced torque controllers for traction and propulsion motors. He is involved in many research projects with industry aimed at technology transfer from academia.



ERIC ARMANDO (Senior Member, IEEE) received the M.Sc. and Ph.D. degrees in electrical engineering from Politecnico di Torino, Turin, Italy, in 2002 and 2008, respectively.

He is currently with Politecnico di Torino as a Full Professor of power converters, electrical machines, and drives. He is the coauthor of numerous journal papers and three patents. His research interests include power electronics and high-performance AC motor drives.

Dr. Armando was the recipient of three awards for innovation, one paper award from the Power Electronics Technical Committee of the IEEE Industrial Electronics Society, and one paper award from the Industrial Drives Committee of the IEEE Industry Applications Society.



RADU BOJOI (Fellow, IEEE) received the M.Sc. degree in electrical engineering from the Technical University of Iasi, Iaşi, Romania, in 1993, and the Ph.D. degree in electrical engineering from Politecnico di Torino, Turin, Italy, in 2002.

He is currently a Full Professor of power electronics and electrical drives with the Energy Department "G. Ferraris," Turin, and the Chairman of the Power Electronics Innovation Center, Politecnico di Torino. He has authored or coauthored more than 200 papers covering electrical drives and power electronics for industrial applications, transportation electrification, power quality, and home appliances. He was involved in many research projects with the industry for direct technology transfer aiming at obtaining new products.

Dr. Bojoi was the corecipient of seven IEEE prize paper awards.